23

Monte Carlo simulations of photoplethysmography and pulse oximetry signals for designing wearable devices

© M.Yu. Kirillin[1,2], D.A. Kurakina[1,2], V.V. Perekatova[1,2], A.A. Serebryakova[1,2], M.A. Sveshnikova[1,2], S.F. Nasrulaev[3], R.V. Gurkin[3], M.V. Ivanchenko[1], E.A. Sergeeva[1,2]

[1] Lobachevsky University of Nizhny Novgorod,
Nizhny Novgorod, Russia
[2] Federal Research Center A.V. Gaponov-Grekhov Institute of Applied Physics
of the Russian Academy of Sciences (IPF RSA),
Nizhny Novgorod, Russia
[3] SberDevices,
Moscow, Russia

e-mail: mkirillin@yandex.ru

Received October 31, 2025
Revised November 07, 2025
Accepted November 25, 2025

This paper employs Monte Carlo numerical simulations to analyze the choice of source-detector distance in the optical scheme of a wearable device designed for photoplethysmography and reflectance-mode pulse oximetry. The simulations were performed for a multilayer medium mimicking human finger biological tissues at three wavelengths: green, red, and infrared.

For each wavelength, the simulation was conducted for both systolic and diastolic phases of the heartbeat. This enabled an analysis of the dependence of the relative heartbeat-induced signal change on the source-detector separation. It is demonstrated that the relative signal change between systolic and diastolic phases increases monotonically with increasing source-detector distance.

Furthermore, the dependence of pulse oximetry calibration curve coefficients on this parameter was identified. Based on the demonstrated effects, recommendations for optimizing the source-detector distance in commercial wearable devices are provided, considering the specified technical characteristics of the optical components.

Keywords: biophotonics, photoplethysmography, pulse oximetry, Monte Carlo simulations.

DOI: 10.61011/EOS.2025.12.63184.46-25

Introduction

Wearable devices are now increasingly used for everyday continuous monitoring of human physiological parameters (heart rate, blood oxygen saturation, sleep, etc.) [1–4], where a significant portion of parameters is estimated based on photoplethysmography (PPG) signals recorded at one or more probing wavelengths [1,5].

Wearable devices typically use reflectance measurements, where the light source and detector are located at a short distance on the inner surface of the device, adjacent to the skin surface. In this they greatly differ from the pulse-oximeters, which traditionally operate in a transmittance configuration and are placed on the distal phalanx of a person's finger or earlobe, in where the modified Beer-Bouguer-Lambert extinction law is used to assess changes in the optical transmittance of biological tissue during blood pulsation. These localizations are characterized by high blood content, but devices with a transmittance configuration in these localizations are uncomfortable for continuous wear, which necessitates the development of a design based on reflectance geometry.

Wearable PPG devices predominantly use configurations involving multiple LEDs, whereas research devices using combinations of two [6,7] to four [8–10] and five [11] wavelengths. Wavelengths of the blue-green range are used to detect the pulse wave, while wavelengths from the red and infrared bands are used to assess blood saturation. Signals at all wavelengths can be detected by one or more photodetectors. A critical structural parameter for these systems is the source-detector distance, which may vary from fractions of a millimeter to several millimeters due to design requirements. Many improvement options for this parameter in commercial and research devices are based on empirical results or simplified models. Thus, in the study [12], the PPG module was improved using modeling based on the Beer-Bouguer-Lambert law to maximize the pulsed-to-constant components ratio in PPG signals.

Apart from the location of the source and detector, the optical characteristics of biological tissues affect the detected blood pulse signal. They exhibit a strong spectral dependence [13], which leads to a difference in physical volume from which the signal is collected (the so-called „measurement volume“) at different probe wavelengths. At the same time, the reconstruction algorithms assume that the measurements at different wavelengths are carried out in the same volume. The measurement volume in biological tissues cannot be determined non-invasively. In

this situation, light propagation models in biological tissues offer a convenient solution to the problem of determining the measurement volume. However, high parameterization of the problem makes it difficult to use analytical models and requires the use of numerical modeling methods. One such approach that takes into account complex morphology of the skin and performs a measurement volume analysis is Monte Carlo statistical method. It is based on the analysis of random photon trajectories and provides the ability to track the depth of penetration of individual photons, providing complete information about the measurement volume.

In this article, we use Monte Carlo method to analyze the formation of a PPG signal in a reflectance configuration for various distances between the source and the detector at wavelengths commonly used in wearable devices. The study was conducted for a multilayer medium that mimics human finger tissue. The source and detector characteristics are close to the typical parameters used in commercial wearable devices [14].

The Monte Carlo method has previously been used to analyze the measurement volume in various configurations of PPG systems [15–17] and to construct calibration curves for pulse oximetry [18,19] using plane-layer models. In [15], a single artery in the skin was considered in the model, and the source-detector distance was optimized for wavelengths of 520 and 612 nm. In most cases, blood pulsation is simulated by creating an additional layer within the tissue that is filled with arterial blood, which models the increase in arterial blood volume during vasodilation [16,18,19]. This model demonstrates a significant change in the probing volume even during a single pulsation period [16]. However, estimates of changes in blood volume in such a model suggest that its use results in an overestimation of the local variation in the optical properties of biological tissue during pulsation. In addition, a continuous layer of arterial blood serves as an „absorbing“ screen, which is not consistent with the actual physiology of the process. In [17], an alternative approach was presented, where pulsation was simulated by doubling the volume of arterial blood in the dermis during systole compared to diastole. Since the typical size of vessels is significantly smaller than the measurement volume of PPG, which is characterized by the source-detector distance [20], a uniform distribution of changes in blood content across the blood-containing layers appears to be the most preferable approach for the systematic analysis. It should be noted that the issue of system analysis in signal formation for a refined biological tissue model in the development of wearable devices optics where multiple probing wavelengths are used remains open. In this paper, the formation of signals in an optical system is analyzed where the principles of PPG and pulse oximetry in a reflectance geometry are used accompanied by examining the probing depth, relative variation of signals, and the shape of the calibration curve for pulse oximetry at different source-detector distances, in order to give recommendations on the choice of these distances when designing the wearable devices. The basic model is based on human finger tissue, similar to [17], but unlike that study, it also takes into account the presence of blood vessels in the hypodermis, where the finger arteries are anatomically located.

Materials and methods

In this study, we have adapted our previously developed Monte Carlo algorithm for calculating reflection spectra in optical diffuse spectroscopy [21] to model the registered photoplethysmogram signal for various probe wavelengths. The realization was previously verified by comparing it with various analytical models [22–24]. The advantage of this realization is the ability to calculate the distribution of probing depths depending on the distance between the source and the detector.

The proposed model allows us to calculate the signals detected by the wearable device's optical system in the reflectance configuration for various source-detector distances. The source and detector parameters are selected based on the typical parameters of wearable devices' optical systems [14]. A configuration with a single source emitting at one of three possible wavelengths (518, 667, or 941 nm) and a single detector was considered. The source size was 1 mm, and the probing beam was considered to be collimated. The detector width was 1 mm, and the numerical aperture of the detector was selected as $NA = 0.85$. The number of photons used in the simulation was 10^{11} for a wavelength of 518 nm and $5 \cdot 10^{10}$ for wavelengths of 667 and 941 nm. To speed up the calculation, the system uses ring detectors that assumes axial symmetry of the problem, which significantly reduces the level of statistical noise during simulation [22]. The distance r between the centers of the source and detector varied from 1 to 9.5 mm with a step of 0.5 mm. The signal intensity $I(r)$, averaged over the area of the real detector, was calculated from the power registered by the ring detector by dividing it by the area of the ring with an average radius r equal to the specified source-detector distance. The configuration scheme of the source and the ring detector with a variable distance between them is illustrated in Fig. 1. In addition to the intensity of the received signal, the model also calculated the density maps of photon trajectories and the distribution of photons $P(z, r)$ over the maximum depths z reached in the medium, for various source-detector distances r [21].

Numerical simulations were performed in the approximation of a plane-layered structure of the object, the layer characteristics of which corresponded to the morphological structures of a human finger, and their optical properties at the required wavelengths were found based on the available data. The realistic and simplified morphology of the human finger used in modeling is illustrated in Figs. 2, *a* and *b*, respectively, while Table 1 shows averaged thicknesses of the tissue layers used in the numerical model of the finger. The total thickness of the finger considered in the modeling was 16 mm and corresponded to the typical size of the proximal phalanx of a female finger without a clamp or

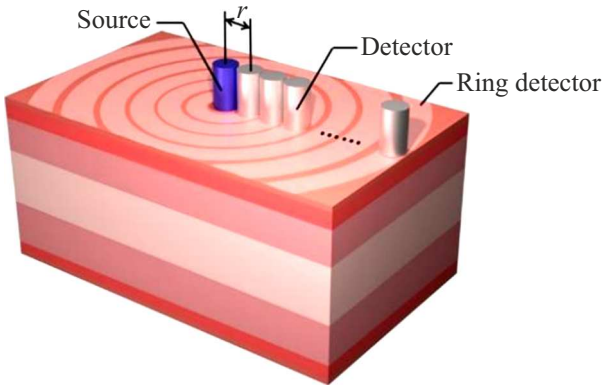

Figure 1. Geometry of source (S) and detector (D) configuration used in the Monte Carlo method. The measurement scheme is given for the palmar side of the finger.

Table 1. Typical layer thicknesses in the problem of radiation propagation in human proximal phalanx tissues

Layers	Thickness, mm
Stratum corneum + epidermis (palmar/back side)	0.2/0.1
Dermis (palmar/back side)	1/1
Hypodermis (palmar/back side)	4.7/1
Tendon (palmar/back side)	3/1
Bone	4
Total	16

a male finger with a clamp, as measured in volunteers (from the research group). The size of the medium in the orthogonal directions was 100 mm to satisfy the condition of a semi-infinite layer. The model takes into account that the palmar side, where the sources and detector are located, has a thicker stratum corneum than the back side.

In this study, we rejected the arterial layer concept, which was used in previous similar model studies [16]. The approach used in this work is similar to that used in [17], but the key difference is that we do not consider the upper and lower plexuses as separate blood layers, but instead assume that the blood is evenly distributed throughout the dermis. This assumption is based on our previous study, where the optoacoustic method was used to show that individual plexuses were clearly visible only in volunteers over the age of 50, and the difference in blood content between the plexuses and the space between them was less than 40% [25]. Moreover, we assume that the hypodermis located deeper than the dermis layer and composed of connective and adipose tissues, also has a non-zero blood content, as it contains the main arteries that run along the entire finger (Fig. 2, *a*). In our simplified geometry, we do not distinguish between arteries as separate structures, replacing them with a uniform distribution of blood throughout the hypodermis layer. This simplification is consistent with the fact that the measurement captures the average contribution from the blood in the arteries.

The optical properties of all selected layers at three wavelengths of the probing radiation are given in Table 2 with references to the corresponding published papers from which they were taken. According to morphological data, the dermis and hypodermis were selected as layers containing blood; the parameters of blood content pulsed changes in these layers were set separately. The possible presence of blood in other structures was considered insignificant and was described by their basic optical properties. The optical properties of the surface layer „stratum corneum + epidermis“ differ between the palmar and back sides, because the epidermis of the palm is the so-called thick skin and contains less melanin than the epidermis of the back side, which is the thin skin.

The following characteristics were introduced to describe the blood-content evolution:

– C_{dia} — background dermis blood content in the diastolic phase, defined as the volume fraction of blood in a given tissue; this value is estimated as the average blood-content of peripheral human tissues;

– StO_{dia} — background saturation of peripheral tissues in the diastolic phase;

– Δ — portion of additional blood-content in the systolic phase, which describes the relative increase in the volume fraction of blood at the moment of the peak of the pulse wave of blood pressure;

– StO_{sys} — arterial blood saturation in the systolic phase of the pulse wave;

– $\mu_{a,\text{HbO}}$ — the absorption coefficient of fully oxygenated blood;

$\mu_{a,\text{Hb}}$ — the absorption coefficient of fully de-oxygenated blood;

These parameters determine the change in absorption coefficients in dermis and hypodermis relative to the values specified in Table 2, which are referred to as $\mu_{a,D}^{(0)}$ and $\mu_{a,Sub}^{(0)}$, respectively.

Dermal absorption coefficient in the diastolic phase $\mu_{a,D}^{(\text{dia})}$:

$$\mu_{a,D}^{(\text{dia})} = \mu_{a,D}^{(0)} + C_{\text{dia}}\left(StO_{\text{dia}}\mu_{a,\text{HbO}} + (1 - StO_{\text{dia}})\mu_{a,\text{Hb}}\right). \quad (1)$$

Hypodermic absorption coefficient in the diastolic phase $\mu_{a,Sub}^{(\text{dia})}$:

$$\mu_{a,Sub}^{(\text{dia})} = \mu_{a,Sub}^{(0)} + 0.5C_{\text{dia}}\left(StO_{\text{dia}}\mu_{a,\text{HbO}} + (1 - StO_{\text{dia}})\mu_{a,\text{Hb}}\right). \quad (2)$$

Peak dermal absorption coefficient in the systolic phase $\mu_{a,D}^{(\text{sys})}$:

$$\mu_{a,D}^{(\text{sys})} = \mu_{a,D}^{(\text{dia})} + \Delta \cdot C_{\text{dia}}\left(StO_{\text{sys}}\mu_{a,\text{HbO}} + (1 - StO_{\text{sys}})\mu_{a,\text{Hb}}\right). \quad (3)$$

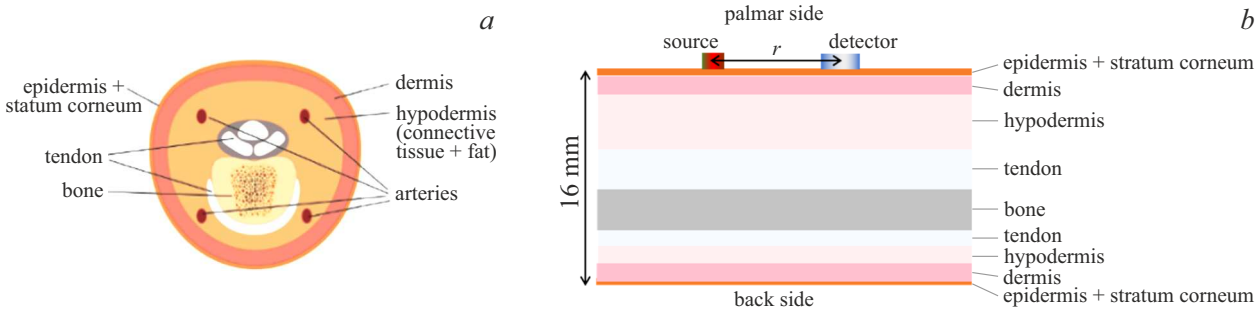

Figure 2. Cross-section diagram of the finger (*a*), a nine-layer planar model of the finger used in simulations (*b*).

Table 2. Optical properties of various layers of biological tissue

Layer	Parameter	Wavelength			References
		518 nm	667 nm	941 nm	
Stratum corneum + epidermis (palmar/back side)	μ_a, mm^{-1}	0.5/0.6	0.2/0.3	0.06/0.1	[16,26,27]
	μ_s, mm^{-1}	28/35	22/25	18/20	[16]
	g	0.77	0.81	0.89	[16]
	n	1.4	1.4	1.4	[28,29]
Bloodless dermis	μ_a, mm^{-1}	0.1	0.07	0.05	[27,30]
	μ_s, mm^{-1}	20	15	10	[16]
	g	0.78	0.82	0.89	[16]
	n	1.4	1.4	1.4	[29]
Bloodless hypodermis (fat and connective tissues)	μ_a, mm^{-1}	0.2	0.1	0.06	[26]
	μ_s, mm^{-1}	6	5.6	5	[16]
	g	0.8	0.85	0.9	[16]
	n	1.4	1.4	1.4	[29]
Tendon	μ_a, mm^{-1}	0.14	0.07	0.05	[29,31]
	μ_s, mm^{-1}	16	12	9	[29]
	g	0.86	0.86	0.86	[32]
	n	1.45	1.45	1.45	[28,29]
Bone	μ_a, mm^{-1}	0.1	0.06	0.03	[29,31]
	μ_s, mm^{-1}	18	16	14	[29]
	g	0.86	0.86	0.86	[32]
	n	1.5	1.5	1.5	[28,29]

Peak hypodermal absorption coefficient in the systolic phase $\mu_{a,Sub}^{(sys)}$:

$$\mu_{a,Sub}^{(sys)} = \mu_{a,Sub}^{(dia)} + 0.5\Delta \cdot C_{sys}\left(StO_{sys}\mu_{a,HbO} + (1 - StO_{sys})\mu_{a,Hb}\right). \quad (4)$$

Table 3 shows the input parameters used in the calculations, their inter-ratios, and the absorption coefficients of oxygenated and deoxygenated blood at the corresponding wavelengths, taken from [33]. Table 4 provides the absorption coefficients in the blood-containing dermis and hypodermis in the diastolic and systolic phases for a given peak saturation $StO_{sys} = 0.98$, as well as the values of effective diffuse light attenuation coefficient $\mu_{ef} = \sqrt{3\mu_a(\mu_a + \mu_s(1-g))}$ for the main morphological layers. This parameter determines the relationship between signal intensity and the distance between the source and the detector. From Table 4 we may see that the most noticeable change in the absorption coefficient between the diastolic and systolic phases occurs at a wavelength of 518 nm — by about 20% in the dermis and by 10% in the hypodermis, and the less noticeable — at a wavelength of 667 nm — within 1–1.5%. The relative change in the effective attenuation coefficient between phases is approximately half the relative change in the absorption coefficient.

When studying the dependence of the backscattering signal on parameters, the results of computational modeling were compared with analytical normalized dependencies of the backscattering signal intensity $I_{theory}(r)$ on distance in a homogeneous semi-infinite layer of biotissue at different wavelengths. To do this, the following model of the

Table 3. Values of some parameters of blood dynamics for different wavelengths

StO_{sys}	Δ	C_{dia}	StO_{dia}	$\mu_{a,HbO}$, mm^{-1}	$\mu_{a,Hb}$, mm^{-1}
				518 nm/667 nm/941 nm	
0.8÷1	0.25	0.02	$StO_{sys}-0.1$	12.61/0.16/0.66	16.74/1.58/0.37

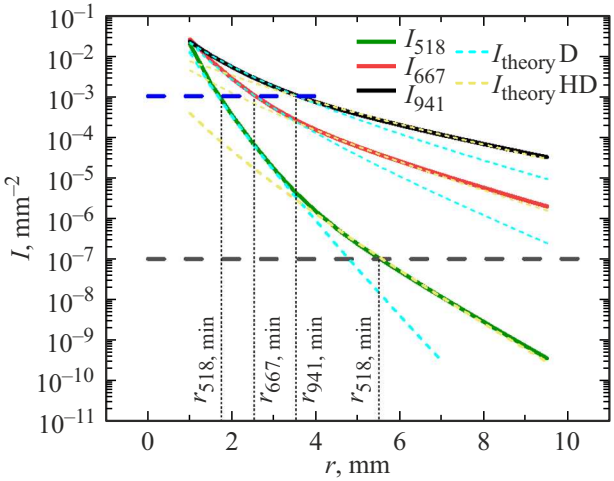

Figure 3. Intensity $I(r)$ of the backscattering signal in diastolic phase versus source-detector distance r at three probing wavelengths for a unit-power source. Colored dashed lines indicate the analytically obtained asymptotics $I_{theory}(r)$ for a semi-infinite layer of dermis (I_{theory} D, cyan) and hypodermis (I_{theory} HD, yellow). The black dashed line indicates the lower limit of the detector's sensitivity $I_{min} = 10^{-7}$. The blue dashed line indicates the estimate of the upper limit of the dynamic range of the photodetector, corresponding to $I_{max} = 10^{-3}$.

backscattering signal intensity was applied for a unit-power source [34]:

$$I_{theory}(r) = \frac{l_t}{4\pi}\left[\left(\mu_{ef} + \frac{1}{\sqrt{r^2 + l_t^2}}\right)\frac{\exp(-\mu_{ef}\sqrt{r^2 + l_t^2})}{r^2 + l_t^2}\right.$$
$$\left. + \frac{7}{3}\left(\mu_{ef} + \frac{1}{\sqrt{r^2 + (7l_t/3)^2}}\right)\frac{\exp(-\mu_{ef}\sqrt{r^2 + (7l_t/3)^2})}{r^2 + (7l_t/3)^2}\right], \quad (5)$$

where $l_t = \mu_a + \mu_s(1-g)$ — transport length.

Results and discussion

Backscattering intensity versus source-detector distance

Fig. 3 illustrates the intensity $I(r)$ of the backscatter signal in diastolic phase versus distance r between the centers of the non-point source and detector for the three wavelengths considered: $I_{518}(r)$ for $\lambda = 518$ nm, $I_{667}(r)$ for $\lambda = 667$ nm and $I_{941}(r)$ for $\lambda = 941$ nm. All dependences are normalized for the source power. It can be seen that in the considered range of values r the signal decay rate varies with distance. This is because of the layered structure of the biological tissue, where the dermis layer has a higher diffuse attenuation coefficient compared to the underlying hypodermis. To confirm this fact, we plotted theoretical normalized dependencies of the backscattering signal intensity $I_{theory}(r)$ on the distance in the semi-infinite dermis and hypodermis layers, using a model described by the formula (5). The slope starts to change at distances of 3.5–4 mm, and we may expect that on the mentioned distances r the measurement volume shifts from the dermis region into the hypodermis region. With a further increase in r, there is no significant change in the slope of the dependencies $I(r)$, which can be attributed to two factors: a slight change in the effective attenuation coefficient in deeper layers, or a minor shift of the measurement volume deeper into the hypodermis as r rises. A detailed study of the location of the sensitivity area for various r will be provided below.

A noticeable difference in the effective attenuation coefficient at three wavelengths for both the dermis and the hypodermis (Table 4) results in a backscattering intensity drop over in studied range of r of 3 orders of magnitude for $\lambda = 941$ nm, 4 orders for $\lambda = 667$ nm and 9 orders for $\lambda = 518$ nm. This decline is particularly critical for $\lambda = 518$ nm, which imposes some conditions on the choice of the source-detector distance. Due to the low average signal $I_{518}(r)$, the dark noise of the photodetector is the main contributor to noise. Typical source power for the wearable device makes about 10–15 mW, while minimal intensity providing a tenfold exceed of the effective signal over the dark photocurrent may be estimated as 0.1 μW/cm^2 [14]. Thus, for the intensity normalized to the power of the source in units of 1/mm^2 , the minimum useful signal level is $I_{min} = 10^{-7}$ and is represented in Fig. 3 as a black dashed line, below which the signal is considered to be insufficient for successful measurement. Another parameter of the photodetector, namely, the magnitude of its dynamic range, can limit the minimum source-detector distance. For a photodetector with parameters described in [14], the maximum level of intensity normalized to the source power in units of 1/mm^2 can be estimated as $I_{max} = 10^{-3}$ and is represented in Fig. 3 as a blue dashed line. Thus, it can be assumed that the source-detector distance for $\lambda = 518$ nm should not exceed $r_{518,max} = 5$ mm, while for the wavelengths of 941 and 667 nm used for measuring arterial blood saturation, dark noise does not limit the maximum source-detector distances. On the other hand, minimal distance r, defined by dynamic range of the detector may be estimated as $r_{518,min} = 1.8$ mm for $\lambda = 518$ nm, $r_{667,min} = 2.5$ mm for $\lambda = 667$ nm and $r_{941,min} = 3.5$ mm for $\lambda = 941$ nm. This limitation can be overcome by reducing the source power.

Table 4. Dermis and hypodermis absorption coefficients for a saturation of $StO_2 = 0.98$ and effective attenuation coefficients of the finger layers for different wavelengths

Parameter	Layer		$\lambda = 518$ nm	$\lambda = 667$ nm	$\lambda = 941$ nm
Absorption coefficient, mm^{-1}	Dermis	$\mu_{a,D}^{(dia)}/\mu_{a,D}^{(sys)}$	0.36/0.42	0.077/0.078	0.062/0.065
	Hypodermis	$\mu_{a,sub}^{(dia)}/\mu_{a,sub}^{(dia)}$	0.33/0.36	0.103/0.104	0.066/0.068
Effective attenuation coefficient, mm^{-1}	Dermis	$\mu_{ef,D}^{(dia)}/\mu_{ef,D}^{(sys)}$	2.27/2.48	0.800/0.805	0.465/0.478
	Hypodermis	$\mu_{ef,sub}^{(dia)}/\mu_{ef,sub}^{(sys)}$	1.23/1.30	0.541/0.542	0.335/0.339
	Tendon	$\mu_{ef,tendon}$	1.00	0.61	0.44
	Bone	$\mu_{ef,bone}$	0.87	0.64	0.42

Analysis of the measurement volume

As shown earlier in a number of studies [17], the probing depth depends on the source-detector distance, and the choice of this parameter is an effective tool for controlling the measurement volume. In case of the reflectance configuration the measurement volume is known to be represented by banana-shape regions. The typical appearance of such regions for the wavelengths under consideration is shown in Fig. 4, which demonstrates an increase in the probing depth as the source-detector distance increases. The maps are presented on a logarithmic scale and are normalized to the maximum value of trajectory density.

Trajectory density maps allow to qualitatively analyze which areas of biological tissue fall within the measurement volume for different wavelengths. For $\lambda = 518$ nm, the depth of the measurement volume increases more slowly with increasing r compared to $\lambda = 667$ nm and $\lambda = 941$ nm, and for $r > 8$ mm, the position of the measurement volumes at the three wavelengths differs significantly. At the same time, the areas of sensitivity remain within the blood-containing layers of the dermis and hypodermis, which simplifies the description of the effect of deeper layers of biological tissue on the formation of the diffuse reflectance signal.

To numerically characterize the position of the measurement volume, the probing depth curves z_{max} were plotted (Fig. 5). This value is calculated as the average of the distribution of photons $P(z, r)$ that arrived at a specific detector at a distance of r,over the maximum depths reached in the medium [21]:

$$z_{max}(r) = \int P(z, r) z dz / \int P(z, r) dz. \qquad (6)$$

Like the trajectory maps, the dependencies $z_{max}(r)$ demonstrate that the dermal and hypodermal layers on the palmar side make the main contribution to signal formation at relevant source-detector distances. The signal from photons reaching the layers on the back side is negligible compared to the signal backscattered from the layers on the palmar side. For the wavelengths of 667 and 941 nm the probing depth shifts from the dermis layer into hypodermis at $r = 2$ mm, while for 518 nm this shift occurs at $r = 3$ mm. Starting from $r = 5$ mm, there is a rising deviation of the curves $z_{max}(r)$ for different wavelengths from each other, with the most pronounced deviation for $\lambda = 518$ nm. This fact illustrates the mutual shift of measurement volumes, which can make it difficult to interpret data obtained at large r.

Analysis of pulse wave characteristics

The passage of the pulse wave is accompanied by variations in the intensity of the diffuse reflectance signal $\Delta I(r)$ due to higher absorption coefficient resulting from an increase in blood volume in the peripheral tissues. The photoplethysmogram recorded during this process is used to determine both the heart rate (usually using wavelengths in the green range) and the oxygen saturation of arterial blood which is traditionally determined using a calibration curve based on the assumption that oxygen saturation is linearly related to the ratio of the signals relative variations at wavelengths of 667 and 941 nm during pulsation. The magnitude of the relative change in the photoplethysmogram signal, $\delta I(r) = |\Delta I(r)|/I(r)$, depends on the choice of source-detector distance, and an important criterion for selection is independence of the derived values from this parameter.

Relative variation of signals $\delta I(r)$ at three wavelengths versus source-detector distance, obtained by Monte Carlo simulation, is presented in Fig. 6. The lowest level of $\delta I(r)$ was observed at 667 nm, which was caused by the lower relative difference $(\delta\mu_{a,D} = \mu_{a,D}^{(sys)}/\mu_{a,D}^{(dia)} - 1)$ between the systolic and diastolic absorption at a given wavelength compared to 941 and 518 nm (Table 4). The amplitude of the pulse wave at 518 nm is a way higher than at two other wavelengths and for larger r the value δI_{518} tends to 1. The dependence $\delta I_{518}(r)$ is characterized by a change of slope near $r = 4$ mm. This effect is particularly associated with a lower relative pulsation change in absorption in the hypodermis, where the measurement volume shifts for $r > 4$ mm, compared to the dermis. For wavelengths of 667 nm and 941 nm, the relative absorption variation in the dermis

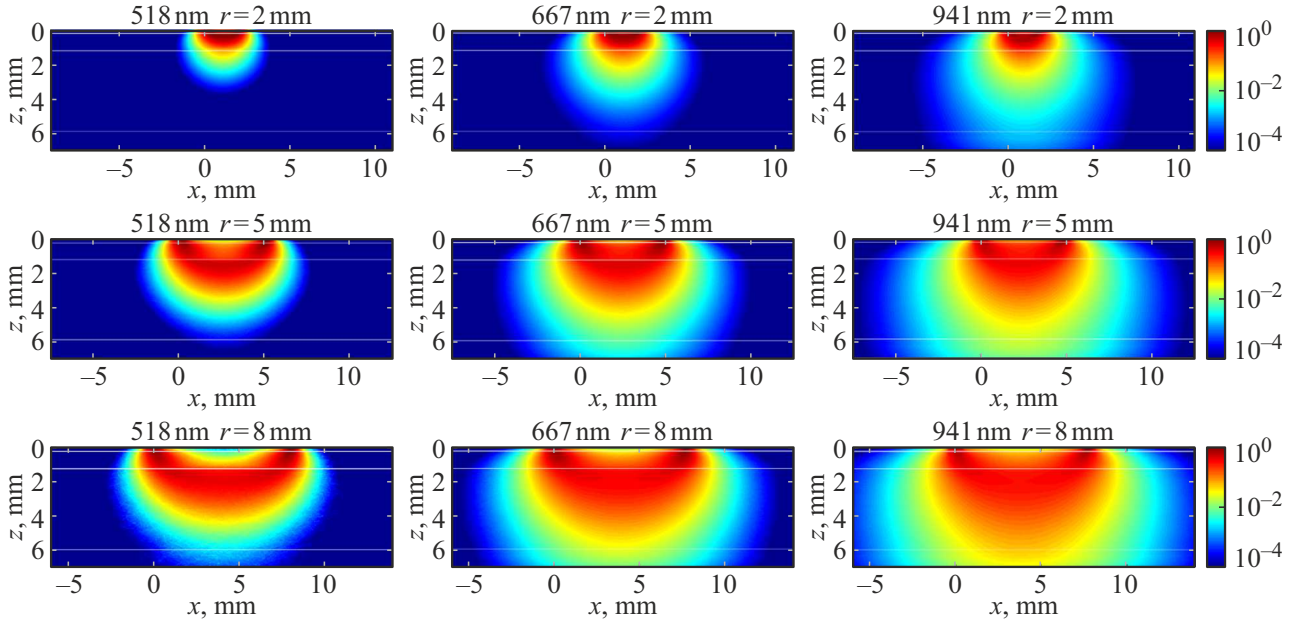

Figure 4. Typical maps of the photons trajectories density (in logarithmic scale) for the three wavelengths and typical source-detector distances $r = 2$, 5 and 8 mm. The white lines correspond to the layer boundaries according to Table 1.

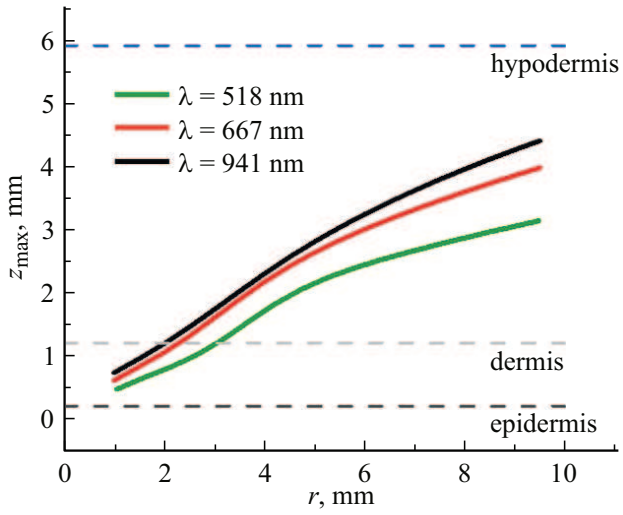

Figure 5. Probing depth z_{max} versus source-detector distance for the three probing wavelengths.

and hypodermis are similar, and there is no significant change in the slope for dependencies $\delta I_{667}(r)$ and $\delta I_{941}(r)$.

The increase in $\delta I_{518}(r)$ combined with the limitation of the average signal level $I_{518}(r)$ due to receiver noise allows determining the optimal source-detector distances when only the pulse wave needs to be measured. In the range of $r = 3-5$ mm, the pulse wave has both a high amplitude and a sufficient average signal level. It should be noted that large pulse wave amplitudes are due to the fact that the model accounts for maximum change in arterial blood volume during pulsation, which actually corresponds to the maximum possible registered change, and this value will be significantly smaller under normal conditions.

Analysis of the saturation calibration versus source-detector distance

To assess arterial blood saturation, a pair of wavelengths from the red and infrared ranges is conventionally used, where the absorption of oxy- and deoxyhemoglobin differs significantly. Saturation is quantified from the ratio of relative changes in signals at two wavelengths $R = \delta I_{667}/\delta I_{941}$ using an empirically or numerically derived calibration curve [17,35]. The dependence of R on the source-detector distance is illustrated in Fig. 7 for various values of arterial blood saturation from the physiological range. From the demonstrated dependence, we can see that for any saturation value, this value is not invariant with respect to the source-detector distance.

The results suggest that the calibration curve for pulse oximetry in reflectance geometry may also depend on the selected source-detector distance, and if the calibration curves are used neglecting the specific system configuration it may lead to errors in saturation determination.

To identify the dependence of the calibration curve parameters on the source-detector distance the ratio between the arterial blood saturation StO_2 and the value $R = \delta I_{667}/\delta I_{941}$ was approximated by a linear function with coefficients a and b, defined for each value r [35]:

$$StO_2 = a(r)R + b(r). \quad (7)$$

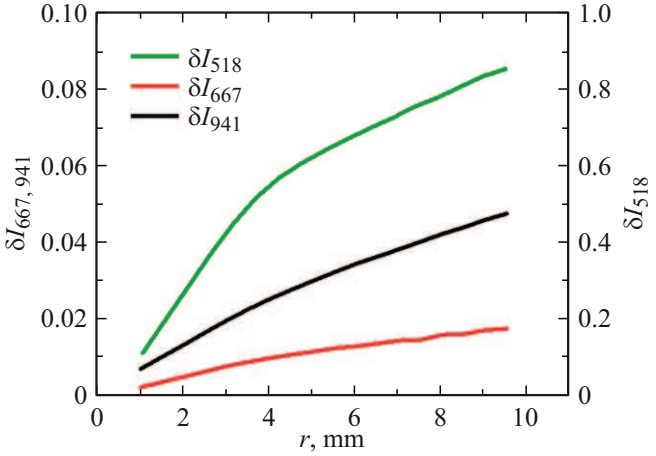

Figure 6. Relative signal variation during pulsation $\delta I(r)$ versus source-detector distance r at three probing wavelengths.

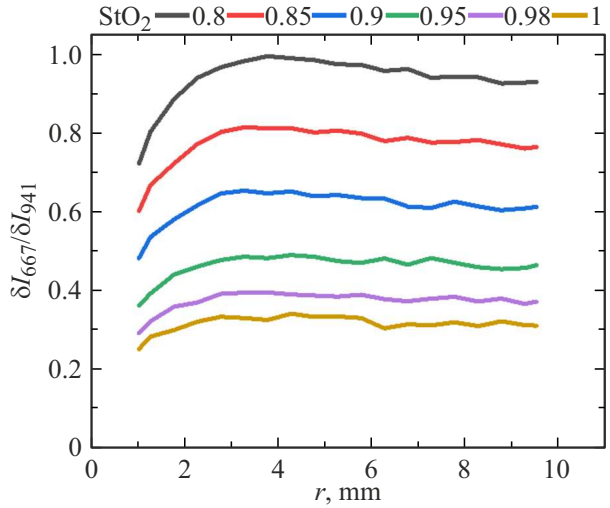

Figure 7. $R = \delta I_{667}/\delta I_{941}$ versus source-detector distance for various saturation of arterial blood within the physiological range.

Parameters a and b versus source-detector distance are shown in Fig. 8. From this figure, we can see that the parameter b is almost independent of r, while the parameter a, which determines the slope of the calibration curve, changes greatly with distance. Variation of $a(r)$ is most pronounced within $r = 1-3.5$ mm, while for $r > 3.5$ mm this dependence is insufficient, yet, it is required to note the declining trend. In this regard, the choice of the distance $r > 3.5$ mm is more preferable for pulse oximetry using wavelengths in the red and infrared ranges, which is consistent with the estimation of the minimum distances $r_{667,\min}$ and $r_{941,\min}$ based on the upper limit of the detector's dynamic range.

When comparing the absolute values of the coefficient b with the values used earlier in the calibration curves, we can see that it is almost the same for the results obtained in this work and the results obtained earlier

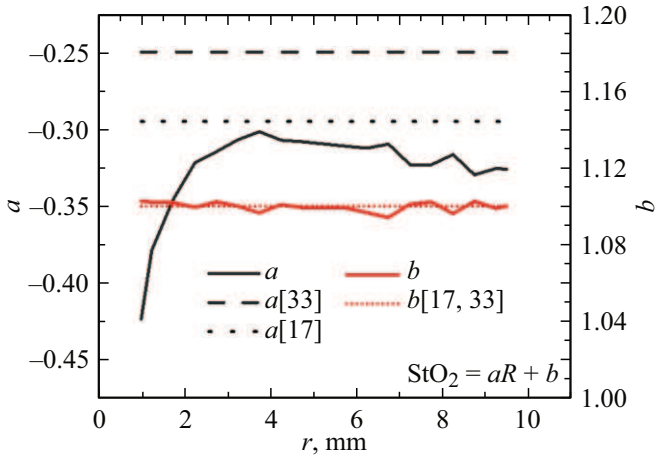

Figure 8. Coefficients a and b of the linear approximation of the calibration curve (6) in the reflectance geometry versus source-detector distance.

in [17,35]. Concerning a coefficient, the study [17] showed that this coefficient in Monte Carlo simulation for a multi-layer model was lower than in the earlier published calibration curve [35]. Parameters a and b from the cited literature are shown in Fig. 8 by dashed lines. The values of coefficient a, obtained in this study are consistent with that from [17], and for the source-detector distances above 2.5 mm, they differ from it by no more than 10 %.

Conclusion

A systematic study of the formation of photoplethysmography and pulse oximetry signals in a reflectance optical system of a wearable device with three probing wavelengths in the green (518 nm), red (667 nm), and near-infrared (941 nm) ranges was conducted. The study was conducted using numerical simulations of the registered backscattering signals by Monte Carlo method, which allowed to analyze the dependence of the typical probing depth on the source-detector distance (r) and compare it with the boundaries of the morphological layers of the tissue: epidermis, dermis, and hypodermis. It was demonstrated, in particular, for the wavelengths 667 and 941 nm that the probing depth shifts from the dermis into hypodermis at $r = 2$ mm, whereas for 518 nm this shift occurs at the distance of $r = 3$ mm. The study of the detected signal intensity as a function of r also showed that in the given range of values r, the signal is mainly influenced by the dermis and hypodermis layers, which was confirmed by the analytical asymptotes of the signal intensity as a function of r in a homogeneous layer with the parameters of the dermis and hypodermis, respectively.

Analysis of the signals relative variation in the systolic and diastolic phases showed a monotonic rise in the relative

variation with an increase in r, which is a clear evidence of a high potential of relatively large source-detector distances with sufficient detector sensitivity. After comparing the findings with the characteristics of available commercial microchips for photoplethysmography it was found that a pretty high sensitivity of the detector could be expected for the red and IR region wavelengths in almost the entire range of the considered distances, whereas for the wavelength of the green band, the ultimate distances were limited due to the dark noise of 5–6 mm.

A relevant issue is the dependence of the calibration curve in pulse oximetry on the configuration of the optical system in reflectance geometry. The study showed that $R = \delta I_{667}/\delta I_{941}$ depends on the source-detector distance, which indicates the need for individual calibration for a given configuration of a wearable device and potential presence of error when using universal calibration formulas. Approximation of the dependence of R on arterial blood saturation by a linear function showed that the coefficient b responsible for the constant part, was practically invariant with respect to the source-detector distance, while the coefficient a accounting for the slope of the linear fit, demonstrates a significant dependence on r. This dependence is most significant in the range of distances r below 3.5 mm, which indicates the need to choose larger source-detector distances to ensure the universality of the calibration curve, even if the source power provides a signal level within the dynamic range of the detector for distances less than 3.5 mm.

In discussing the dependence of the obtained results on individual parameters that may vary for different people, the following should be noted. In the considered device localization area, the most variable parameter is the thickness of epidermis, which also includes the thickness of the stratum corneum of a thick skin. However, this layer is not blood-filled and can be considered as an attenuation filter for the detected signal [24]. Thus, variation of this parameter will not affect the relative values that are studied here. A change in the dermis thickness can obviously affect the ratio of the contributions from the dermis and hypodermis to the detected signal and affect the characteristic source-detector distance at which the contribution from the hypodermis begins to dominate over the contribution from the dermis in signal formation, which in this model corresponds to a value of about 4 mm.

Thus, Monte Carlo computational modeling of backscattering signals enabled to identify the morphological layers of a heterogeneous biotissue that are essential for signal formation, as well as to formulate a number of recommendations for selecting the source-detector distance in the optical system of wearable devices.

Acknowledgments

The authors are grateful to V.V. Dremin and A.V. Dunaev for useful discussions.

Funding

The study was supported by the Ministry of Economic Development of the Russian Federation (Grant Agreement № 139-15-2025-004 of 17 April 2025, IGK 000000Ts313925P3X0002) and PJSC Sberbank (contract #50004802685 of 20.12.2023).

Conflict of interest

The authors declare no conflict of interest.

References

[1] D. Castaneda, A. Esparza, M. Ghamari, C. Soltanpur, H. Nazeran. Int. J. Biosens. Bioelectron., **4** (4), 195–202 (2018). DOI: 10.15406/ijbsbe.2018.04.00125

[2] D. Dias, J. Paulo Silva Cunha. Sensors (Basel), **18** (8), (2018). DOI: 10.3390/s18082414

[3] S. Park, S. Jayaraman. IEEE Eng. Med. Biol. Mag., **22** (3), 41–8 (2003). DOI: 10.1109/memb.2003.1213625

[4] G. Prieto-Avalos, N.A. Cruz-Ramos, G. Alor-Hernandez, J.L. Sanchez-Cervantes, L. Rodriguez-Mazahua, L.R. Guarneros-Nolasco. Biosensors (Basel), **12** (5), (2022). DOI: 10.3390/bios12050292

[5] D. Ray, T. Collins, S. Woolley, P. Ponnapalli. IEEE Rev. Biomed. Eng., **16**, 136–151 (2023). DOI: 10.1109/RBME.2021.3121476

[6] A. Boukhayma, A. Barison, S. Haddad, A. Caizzone. IEEE Access, **9**, 127217–127225 (2021). DOI: 10.1109/ACCESS.2021.3111956

[7] K.M. Warren, J.R. Harvey, K.H. Chon, Y. Mendelson. Sensors (Basel), **16** (3), (2016). DOI: 10.3390/s16030342

[8] S. Han, D. Roh, J. Park, H. Shin. Sensors (Basel), **19** (24), (2019). DOI: 10.3390/s19245441

[9] L. Yan, S. Hu, A. Alzahrani, S. Alharbi, P. Blanos. Biosensors (Basel), **7** (2), (2017). DOI: 10.3390/bios7020022

[10] J. Liu, B.P. Yan, W.X. Dai, X.R. Ding, Y.T. Zhang, N. Zhao. Biomed. Opt. Express, **7** (10), 4313–4326 (2016). DOI: 10.1364/BOE.7.004313

[11] C.T. Hsiao, C. Tong, G.L. Cote. Biosensors (Basel), **15** (4), (2025). DOI: 10.3390/bios15040208

[12] Y.-H. Kao, P.C.-P. Chao, C.-L. Wey. IEEE J. Selected Topics in Quant. Electron., **25** (1), 1–10 (2018). DOI: 10.1109/JSTQE.2018.2871604

[13] V.V. Tuchin, V. Tuchin. *Tissue Optics: Light Scattering Methods and Instruments for Medical Diagnosis* (SPIE Optical Engineering Press, 2000).

[14] *OSRAM SFH-7072 Datasheet* [Electronic resource]. URL: https://look.ams-osram.com/m/682b32d8c8dd3713/original/SFH-7072.pdf

[15] E.F. Pribadi, R.K. Pandey, P.C.-P. Chao. Microsystem Technologies, **26** (11), 3409–3420 (2020). DOI: 10.1007/s00542-020-04895-6

[16] V. Dremin, E. Zherebtsov, A. Bykov, A. Popov, A. Doronin, I. Meglinski. Appl. Opt., **58** (34), 9398–9405 (2019). DOI: 10.1364/AO.58.009398

[17] S. Chatterjee, P.A. Kyriacou. Sensors (Basel), **19** (4), (2019). DOI: 10.3390/s19040789

[18] A. Doronin, I. Fine, I. Meglinski. Laser Physics, **21** (11), 1972–1977 (2011). DOI: 10.1134/S1054660X11190078

[19] L. Hernandez-Quintanar, D.A. Fabila-Bustos, M. Hernandez-Chavez, A. Valor, J.M. de la Rosa, S. Stolik. Comput Methods Programs Biomed., **187**, 105237 (2020). DOI: 10.1016/j.cmpb.2019.105237
[20] E.V. Zharkikh, V.V. Dremin, A.V. Dunaev. J. Biophotonics, **16** (9), e202300139 (2023). DOI: 10.1002/jbio.202300139
[21] D. Kurakina, V. Perekatova, E. Sergeeva, A. Kostyuk, I. Turchin, M. Kirillin. Laser Phys. Lett., **19** (3), 035602 (2022). DOI: 10.1088/1612-202X/ac4be8
[22] E. Sergeeva, D. Kurakina, I. Turchin, M. Kirillin. J. Innovative Optical Health Sciences, **17** (05), 2342002 (2024). DOI: 10.1142/S1793545823420026
[23] V. Perekatova, E. Sergeeva, M. Kirillin, A. Khilov, D. Kurakina, I. Turchin. Opt. Commun., **579**, 131440 (2025). DOI: 10.1016/j.optcom.2024.131440
[24] E.A. Sergeeva, D.A. Kurakina, A.A. Getmanskaya, and M.Yu. Kirillin. Opt. i spektr., **133**, 12 (2025) (in Russian).
[25] V. Perekatova, M. Kirillin, S. Nemirova, A. Orlova, A. Kurnikov, A. Khilov, K. Pavlova, V. Kazakov, V. Vildanov, I. Turchin, P. Subochev. Photonics, **9** (7), 482 (2022). DOI: 10.3390/photonics9070482
[26] E. Salomatina, B. Jiang, J. Novak, A.N. Yaroslavsky. J. Biomed. Opt., **11** (6), 064026 (2006). DOI: 10.1117/1.2398928
[27] Y. Shimojo, T. Nishimura, H. Hazama, T. Ozawa, K. Awazu. J. Biomed. Opt., **25** (4), 1–14 (2020). DOI: 10.1117/1.JBO.25.4.045002
[28] R. Khan, B. Gul, S. Khan, H. Nisar, I. Ahmad. Photodiagnosis Photodyn. Ther., **33**, 102192 (2021). DOI: 10.1016/j.pdpdt.2021.102192
[29] A.N. Bashkatov, E.A. Genina, V.V. Tuchin. J. Innovat. Opt. Health Sciences, **4** (01), 9–38 (2011). DOI: 10.1142/S1793545811001319
[30] T. Kono, J. Yamada. Intern. J. Thermophysics, **40** (5), 51 (2019).
[31] J.L. Sandell, T.C. Zhu. J. Biophotonics, **4** (11–12), 773–87 (2011). DOI: 10.1002/jbio.201100062
[32] S.L. Jacques. Phys. Med. Biol., **58** (11), R37–61 (2013). DOI: 10.1088/0031-9155/58/11/R37
[33] *Optical Absorption of Hemoglobin* [Electronic resource]. URL: https://omlc.org/spectra/hemoglobin/
[34] T.J. Farrell, M.S. Patterson, B. Wilson. Med. Phys., **19** (4), 879–88 (1992). DOI: 10.1118/1.596777
[35] J.T.B. Moyle. *Pulse Oximetry* (BMJ Books, London, UK, 1994).

Translated by J.Savelyeva